

## Scale dependence of kinetic helicity and selection of the axial dipole in rapidly rotating dynamos

Binod Sreenivasan\* and Subhajit Kar

*Centre for Earth Sciences, Indian Institute of Science, Bangalore 560 012, India*



(Received 9 January 2018; published 4 September 2018)

The dominant polarity of the magnetic field in rapidly rotating spherical dynamos is the axial dipole. Studies of the onset of magnetoconvection in the limit of vanishing Ekman number have proposed that the dipole is favored over other polarities because its equatorial symmetry generates kinetic helicity that would be otherwise absent in nonmagnetic convection. This study explores the effect of the magnetic field in the selection of the axial dipole in rapidly rotating, supercritical dynamos. The strength of convection is such that the axial dipole grows from a starting seed field in the nonlinear dynamo but fails to grow in the kinematic dynamo at the same parameters. The magnetic field is shown to excite convection over a range of length scales larger than the energy injection scale and at the same time extract energy from smaller scales through the Lorentz force in order to feed itself. This leads to substantial helicity generation in a range of length scales and helicity loss in smaller scales, both relative to nonmagnetic convection. The crossover point between the helicity surplus and deficit regions is displaced to smaller length scales as the rotation rate is increased (by decreasing the Ekman number). The helicity deficit occurs in the region of the spectrum where the Lorentz force approximately balances the Coriolis force in the vorticity equation, so that energy may be drawn from these scales via vortex stretching. The timescale for the increase in convection intensity relative to the nonmagnetic state approximately coincides with the timescale for the formation of the axial dipole, which indicates that the Lorentz force has an important role in polarity selection. Crucially, the dipole forms from a chaotic state well before the saturation of the dynamo, implying that planetary dynamos choose their polarity during their nonlinear growth phase. The generation of the toroidal part of the dipole field is primarily through the classical  $\Omega$  effect, although the pattern of the zonal flow switches from spherical harmonic degree  $l = 1$  to  $l = 3$  in the presence of the magnetic backreaction.

DOI: [10.1103/PhysRevFluids.3.093801](https://doi.org/10.1103/PhysRevFluids.3.093801)

### I. INTRODUCTION

Planetary dynamos are driven by convective motion in their fluid cores. Considerable progress has been made in modeling thermochemical convection in rapidly rotating spherical shells and their consequences for dynamo action; see, for example, recent reviews [1,2]. Studies of convection-driven dynamos show that different polarities of the magnetic field may be generated, such as the axial dipole, quadrupole [3,4], and the equatorial dipole [5,6]. However, the axial dipole dominates a wide range of the parameter space where the nonlinear inertial term is negligible in the equation of motion [7]. Estimates of the core flow velocity [1] suggest that inertia is important only at very small length scales where magnetic diffusion is rapid, so it is plausible that the axial dipole structure is supported by relatively larger length scales where inertia is small. Recent simulations of strongly driven and

\*bsreeni@iisc.ac.in

rapidly rotating spherical dynamos [8,9] lend credence to the view that the axial dipole would be favored in the Earth-like parameter regime of low Ekman number  $E$  and low magnetic Prandtl number  $Pm$ .

The long-time structure of the convection in spherical geometry is that of columns parallel to the rotation axis (e.g., Refs. [10,11]). While the presence of differential rotation and meridional circulation in the flow may promote dynamo generation of magnetic fields containing an axial dipole [12], it is not certain that the preference for the axial dipole in nonlinear dynamos is due to purely kinematic processes. Rotating kinematic dynamo models at low Ekman number ( $E = 10^{-8}$ ) and low magnetic Prandtl number ( $Pm = 0.005$ ) [13] favor quadrupolar modes over dipolar modes, even though the  $z$  velocity has the same equatorial symmetry as that for convection-driven flow in rotating spherical geometry. Sreenivasan and Jones [14] examine the differences in the patterns of magnetoconvection with dipolar and quadrupolar fields. The presence of an axial dipole gives rise to enhanced velocity gradients  $\partial u_z / \partial z$  above and below the equator via the  $z$ -vorticity equation, and the in-phase relation between the velocity and vorticity produces enhanced helicity compared with that found with quadrupolar fields or in nonmagnetic convection. The presence of helicity in columnar convection is thought to be an important ingredient for dynamo action, and its relation to the  $\alpha$  effect that generates the poloidal magnetic field from the toroidal field is well known [15,16]. The enhancement in axial strain rate by the magnetic field is clearly visible in rotating dynamo simulations at moderate Ekman number ( $E = 3 \times 10^{-4}$ ), although its effect is not a global enhancement in helicity, but an asymmetry in the helicity between cyclonic and anticyclonic vortices that form in rotating convection [17]. The effect of the Lorentz force in extracting energy from cyclonic vortices to feed the magnetic field—while not significantly changing the anticyclonic flow—can partly explain why dynamo models have not shown much global enhancement in helicity over the equivalent nonmagnetic states [18]. The possible exceptions are dynamo models with stress-free boundaries [14], where the magnetic field produces more coherent columnar ( $s, z$ ) helicity in the dynamo than that in nonmagnetic convection, an effect that seems to diminish with large Prandtl numbers as well as with no-slip boundaries. The important question that arises here is whether the dynamo magnetic field in general promotes helical fluid motions in regions that are quiescent in nonmagnetic convection. Plane layer linear magnetoconvection with spatially varying mean magnetic fields [19] offers some insight: Convection is excited in regions where the field is strongest, even when the field intensity is small and the length scale of the flow at onset is viscously controlled. Although the analysis of linear magnetoconvection is restricted by its two length scales—namely the length scale of the field variation and the length scale of convective onset—the above result has the wider implication that the field can substantially promote convection at length scales where the primary balance in the equation of motion does not include the Lorentz force. Recent studies [20,21] indicate that the Lorentz force balances the ageostrophic part of the Coriolis force only at small length scales (or large spherical harmonic degrees) of the dynamo. That having been said, the effect of the magnetic field on helicity production at length scales in the neighborhood of the energy injection scale cannot be ruled out. The present study explores this idea by studying columnar flow and its helicity across length scales in rapidly rotating dynamo models. At sufficiently low Ekman numbers, one would expect the range of scales at which helicity is generated and the range of scales at which helicity is attenuated to be clearly delineated.

While considering the role of magnetic backreaction in the selection of the axial dipole, it is essential to know if the changes in the convection pattern are only produced near the point of nonlinear saturation of the dynamo, where the average field strength measured by the Elsasser number is often  $O(1)$  or higher, or with much weaker fields that exist prior to dynamo saturation. This point is addressed by tracking the flow pattern as the dynamo field grows from a small initial seed, the precise structure of which does not affect the final structure of the field.

The magnetic field in strongly supercritical dynamos contain nondipolar harmonics whose cumulative strength would likely be substantially higher than the dipole even if the structure of the field at the core-mantle boundary is dipole dominated. It is not clear from previous analyses that the equatorially antisymmetric, nondipole part of the field would modify the kinetic helicity

distribution in the dynamo. The present study partly addresses this issue by looking at the Lorentz force contribution from the axial dipole and nondipole parts of the field in the vorticity equation.

Finally, this study looks at the generation of the toroidal part of the dipole field and how it is modified by the magnetic field in nonlinear dynamos.

## II. NUMERICAL DYNAMO MODEL

We consider an electrically conducting fluid between two concentric, corotating spherical surfaces that correspond to the inner core boundary (ICB) and the core-mantle boundary (CMB). The ratio of inner to outer radius  $r_i/r_o$  is chosen to be 0.35. For simplicity, it is assumed that the fluid is subject to a thermal buoyancy-driven convection, although the governing equations may also be used to study thermochemical convection using the codensity formulation [22]. The other body forces acting on the fluid are the Lorentz force, arising from the interaction between the induced electric currents and the magnetic fields, and the Coriolis force, originating from the background rotation of the system.

The governing equations considered are those in the usual Boussinesq approximation [23]. Lengths are scaled by the thickness of the spherical shell  $L$ , and time is scaled by the magnetic diffusion time  $L^2/\eta$ , where  $\eta$  is the magnetic diffusivity. The velocity field  $\mathbf{u}$  is scaled by  $\eta/L$ , and the magnetic field  $\mathbf{B}$  is scaled by  $(2\Omega\rho\mu\eta)^{1/2}$ , where  $\Omega$  is the rotation rate,  $\rho$  is the fluid density, and  $\mu$  is the magnetic permeability. The scaled magnetic field, known as the Elsasser number  $\Lambda$ , is an output derived from our dynamo simulations as a root mean square (rms) value, where the mean is a volume average.

The nondimensional magnetohydrodynamic (MHD) equations for velocity, temperature, and magnetic fields are

$$EPm^{-1} \left[ \frac{\partial \mathbf{u}}{\partial t} + (\nabla \times \mathbf{u}) \times \mathbf{u} \right] + \hat{z} \times \mathbf{u} = -\nabla p^* + Pm \Pr^{-1} Ra T \mathbf{r} + (\nabla \times \mathbf{B}) \times \mathbf{B} + E \nabla^2 \mathbf{u}, \quad (1)$$

$$\frac{\partial T}{\partial t} + \mathbf{u} \cdot \nabla T = Pm \Pr^{-1} \nabla^2 T, \quad (2)$$

$$\frac{\partial \mathbf{B}}{\partial t} = \nabla \times (\mathbf{u} \times \mathbf{B}) + \nabla^2 \mathbf{B}, \quad (3)$$

$$\nabla \cdot \mathbf{u} = \nabla \cdot \mathbf{B} = 0. \quad (4)$$

The modified pressure  $p^*$  in Eq. (1) is given by  $p + \frac{1}{2} EPm^{-1} |\mathbf{u}|^2$ . The dimensionless parameters in Eqs. (1)–(3) are the Ekman number,  $E = \nu/2\Omega L^2$  that measures the ratio of viscous to rotational forces, the Prandtl number,  $\Pr = \nu/\kappa$  that gives the ratio of viscous to thermal diffusivities, the magnetic Prandtl number,  $Pm = \nu/\eta$  that gives the ratio of viscous to magnetic diffusivities, and the “modified” Rayleigh number (product of classical Rayleigh number and Ekman number)  $Ra = g_o \alpha \Delta T L / 2\Omega \kappa$ , where  $g_o$  is the gravitational acceleration acting radially inward,  $\alpha$  is the coefficient of thermal expansion,  $\Delta T$  is the superadiabatic temperature difference between the boundaries, and  $\kappa$  is the thermal diffusivity. The basic-state nondimensional temperature distribution is a conventional basal heating  $T_o(r) = \beta/r$ , where  $\beta = r_i r_o$ . The velocity, temperature, and magnetic fields satisfy the no-slip, isothermal, and electrically insulating conditions respectively at the boundaries. Equations (1)–(4) are solved by a dynamo code that uses spherical harmonic expansions in  $(\theta, \phi)$  and finite differences in  $r$  [24]. The radial points are located at the zeros of a Chebyshev polynomial and are therefore dense near the boundaries. In this way, the Ekman boundary layers are adequately resolved using a fewer number of radial points than would otherwise be possible with an equispaced grid.

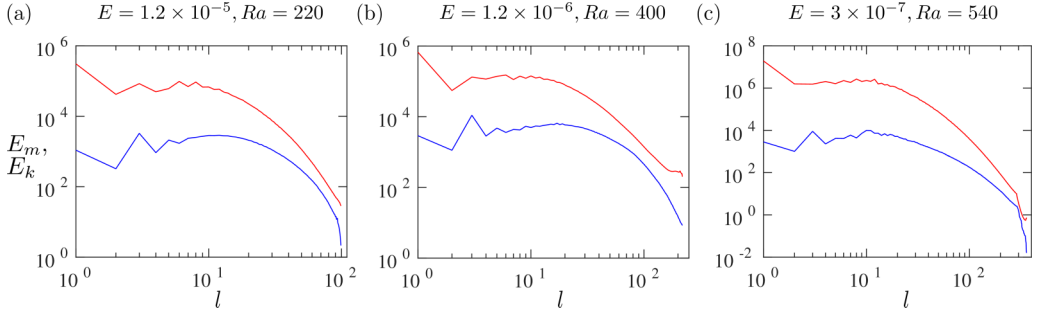


FIG. 1. Time-averaged energy spectra for the nonlinear dynamo simulations, showing the variation of kinetic ( $E_k$ ) and magnetic ( $E_m$ ) energies with spherical harmonic degree  $l$ . The red lines show  $E_m$  and the blue lines show  $E_k$ .

### III. RESULTS

Three parameter regimes are analyzed in this study. For the Ekman numbers  $E = 1.2 \times 10^{-6}$  and  $E = 3 \times 10^{-7}$ ,  $\text{Pr}$  and  $\text{Pm}$  are chosen to be unity, whereas for the relatively higher  $E = 1.2 \times 10^{-5}$ , low nonlinear inertia is ensured by choosing  $\text{Pr} = \text{Pm} = 5$  (e.g., Ref. [7]). The Rayleigh number  $\text{Ra}$  needs to be sufficiently supercritical in order to bring out the effect of the magnetic backreaction in the dynamo process (see below). Figure 1 gives the time-averaged kinetic and magnetic energy spectra in the saturated dynamo state for the three parameter regimes. The saturated state is averaged over approximately 0.3 magnetic diffusion times for  $E = 3 \times 10^{-7}$  and 2 magnetic diffusion times for higher  $E$ . Table I summarizes the nonlinear dynamo simulations performed and their key parameters. Apart from the dimensionless parameters described above, the mean spherical harmonic degrees for convection and energy injection, denoted by  $l_C$  and  $l_E$  respectively, are given by [17,25]

$$l_C = \frac{\sum_l l E_k(l)}{\sum_l E_k(l)}, \quad l_E = \frac{\sum_l l E_T(l)}{\sum_l E_T(l)}, \quad (5)$$

where  $E_k(l)$  is the kinetic energy spectrum and  $E_T(l)$  is the spectrum obtained from the product of the transform of  $u_r T$  and its conjugate.

For each dynamo run, a nonmagnetic calculation at the same  $E$ ,  $\text{Ra}$ , and  $\text{Pr}$  serves as the reference state. The dynamo calculation is started from a seed axial dipole-dominated magnetic field of Elsasser number  $\Lambda = 0.01$  similar to that in Ref. [14] sitting in a velocity field obtained from the reference nonmagnetic state. The growth of the magnetic field and the accompanying changes in the velocity field are studied. For each nonlinear dynamo run, an equivalent “kinematic” run is performed where

TABLE I. Summary of the nonlinear dynamo simulations considered in this study. Here,  $E$  is the Ekman number,  $\text{Ra}$  is the modified Rayleigh number,  $\text{Ra}_c$  is the critical Rayleigh number for onset of convection,  $\text{Pr}$  and  $\text{Pm}$  are the thermal and magnetic Prandtl numbers,  $l_{\max}$  is the maximum spherical harmonic degree,  $N_r$  is the number of radial grid points,  $\Lambda$  is the Elsasser number based on the volume-averaged magnetic field in the spherical shell,  $\Lambda_D$  denotes the dipole Elsasser number computed from magnetic energy contained in the harmonics  $\mathbf{B}_{10}^P$  and  $\mathbf{B}_{20}^T$ ,  $\text{Rm}$  is the magnetic Reynolds number,  $l_C$  is the mean harmonic degree of convective motion, and  $l_E$  is the mean harmonic degree at which energy is injected by buoyancy. The values given within brackets are those for the kinematic calculations where the Lorentz force is zero.

$E$	$\text{Pr}, \text{Pm}$	$\text{Ra}$	$\text{Ra}/\text{Ra}_c$	$l_{\max}$	$N_r$	$\Lambda$	$\Lambda_D$	$\text{Rm}$	$l_C$	$l_E$
$1.2 \times 10^{-5}$	5	220	$\approx 4.5$	100	120	0.70	0.34	102.4 (123.5)	21 (28)	20 (29)
$1.2 \times 10^{-6}$	1	400	$\approx 7.8$	220	220	0.83	0.41	206.8 (265.6)	38 (43)	31 (49)
$3 \times 10^{-7}$	1	540	$\approx 6.6$	320	360	1.56	0.52	216 (358)	54 (64)	48 (70)

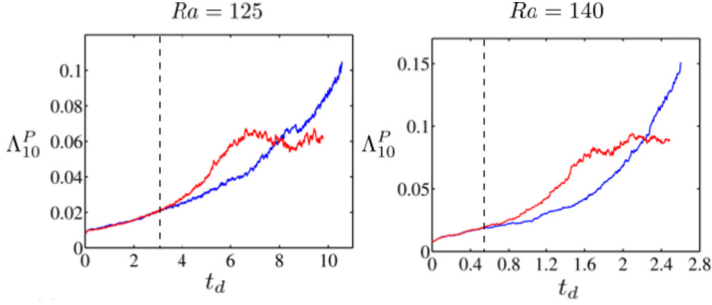


FIG. 2. (a) Evolution in time (measured in units of the magnetic diffusion time) of the axial dipole ( $\mathbf{B}_{10}^P$ ) Elsasser number in nonlinear (red line) and kinematic (blue line) dynamo simulations at  $E = 1.2 \times 10^{-5}$ ,  $\text{Pr} = \text{Pm} = 5$ , and two Rayleigh numbers.

the Lorentz force is set to zero in the equation of motion, as in some previous studies [6,26]. For low-moderate Ra above critical, the poloidal part of the axial dipole field ( $\mathbf{B}_{10}^P$ ) shows a monotonic increase in the kinematic case and an increase followed by saturation in the nonlinear case. In such a situation, one might conclude that the role of the Lorentz force is essentially in dynamo saturation. However, if Ra is sufficiently large, the kinematic run shows no significant increase in  $\mathbf{B}_{10}^P$ , whereas the nonlinear run shows a clear growth of this component. This indicates that the Lorentz force has an important role in the selection of the dipole itself apart from the eventual saturation of the dynamo. To bring out this effect of the Lorentz force, Ra is chosen such that  $\mathbf{B}_{10}^P$  evolves very differently in the nonlinear and kinematic runs.

### A. Selection of the axial dipole

For  $E = 1.2 \times 10^{-5}$ , both the nonlinear and kinematic dynamo runs at Rayleigh numbers  $\text{Ra} = 2.5\text{--}3 \times \text{Ra}_c$  show an increase for  $\mathbf{B}_{10}^P$  (Fig. 2). For  $\text{Ra} = 125$ , this field component grows identically in the two runs until  $\approx 3$  magnetic diffusion times, after which the nonlinear field deviates from the kinematic field and saturates. For  $\text{Ra} = 140$ , the two runs overlap only until  $\approx 0.6$  diffusion time. At these Ra, it is found that the radial magnetic field at the outer boundary retains its dominant dipole structure in both the nonlinear and kinematic runs. As the aim of this study is to identify the effect of the Lorentz force on the growth phase of the dynamo, the Rayleigh number needs to be set to a sufficiently high value ( $\text{Ra} = 220$ ) so that there is no kinematic growth of  $\mathbf{B}_{10}^P$  from the starting seed field [Fig. 3(b)]. Likewise, for the lower Ekman number ( $E = 1.2 \times 10^{-6}$ ), the choice of  $\text{Ra} = 400$  ensures that  $\mathbf{B}_{10}^P$  clearly increases in the nonlinear run but fails to pick up strength in the kinematic run [Fig. 3(c)]. Here, the kinematic growth of the dynamo is entirely from the growth of the nondipole part of the magnetic field, consistent with the video `Br_kin.avi` in the Supplemental Material [27] that shows the radial magnetic field at the outer boundary.

Figure 4 shows the radial field  $B_r$  on the core surface (outer boundary) in the nonlinear dynamo simulations, and the snapshots in Figs. 4(a)–4(e) and 4(f)–4(j) being marked on the Elsasser number plots in Fig. 3(a). As the field grows from its initial seed dipole state, it loses its dipole character but subsequently regains it well before the saturated phase. It is notable that Figs. 4(d) at  $E = 1.2 \times 10^{-5}$  and 4(i) at  $E = 1.2 \times 10^{-6}$ , representing the times at which the axial dipole symmetry is regained, are situated in the rising phase of the magnetic field in Fig. 3(a). That is, the selection of the axial dipole occurs well before dynamo saturation, when the Lorentz force exceeds a threshold value. The video `Br_nl.avi` in the Supplemental Material [28] that accompanies this paper shows the evolution of  $B_r$  in the nonlinear run at  $E = 1.2 \times 10^{-6}$ . Starting from a seed axial dipole, the early loss and subsequent restoration of the dipole symmetry is evident from this video. The axial dipole forms immediately after the time marked by the red vertical line on the Elsasser number plot in the video, well before saturation. In contrast, the video `Br_kin.avi` [27] shows the absence of dipole

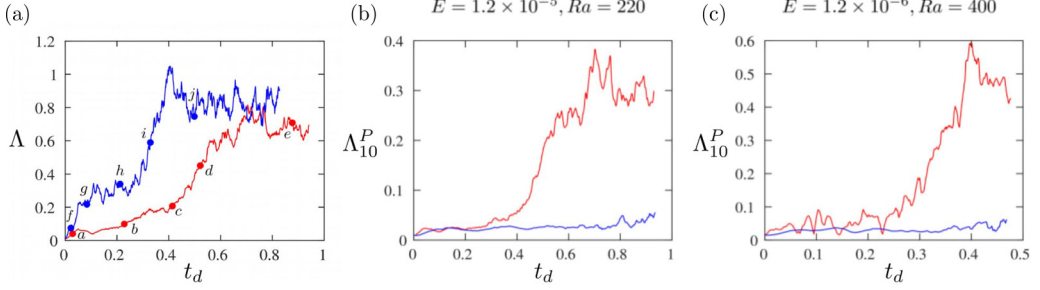


FIG. 3. (a) Evolution in time (measured in units of the magnetic diffusion time) of the Elsasser number in nonlinear dynamo simulations at  $E = 1.2 \times 10^{-5}$ ,  $\text{Pr} = \text{Pm} = 5$ ,  $\text{Ra} = 220$  (red line) and  $E = 1.2 \times 10^{-6}$ ,  $\text{Pr} = \text{Pm} = 1$ ,  $\text{Ra} = 400$  (blue line). The alphabet labels represent the snapshots in time given in Fig. 4 below. (b) Comparison of the axial dipole ( $\mathbf{B}_{10}^P$ ) Elsasser numbers for the nonlinear (red line) and kinematic (blue line) dynamo runs at  $\text{Ra} = 1.2 \times 10^{-5}$ ,  $\text{Ra} = 220$ ,  $\text{Pr} = \text{Pm} = 5$ . (c) Comparison of the axial dipole ( $\mathbf{B}_{10}^P$ ) Elsasser numbers for the nonlinear (red line) and kinematic (blue run) dynamo runs at  $\text{Ra} = 1.2 \times 10^{-6}$ ,  $\text{Ra} = 400$ ,  $\text{Pr} = \text{Pm} = 1$ .

symmetry in the kinematic run at  $E = 1.2 \times 10^{-6}$ , in line with the fact that  $\mathbf{B}_{10}^P$  does not gain in strength in this run.

When the onset of convection occurs near the inner core boundary,  $u_z$  and  $u_s$  are of the same order of magnitude in the  $E \rightarrow 0$  limit, whereas  $u_\phi$  is  $O(E^{1/9})$  smaller [14]. As the Lorentz force is expected to further damp the azimuthal motions, the backreaction of the magnetic field and its scale dependence is measured by first calculating the  $z$  and  $s$  kinetic energy densities as a function of the spherical harmonic degree  $l$  for the nonlinear dynamo. Although the saturated dynamo phase is taken for the purpose of computing time averages, the results are useful in understanding the magnetic backreaction in the growth phase of the dynamo. A similar average over thermal diffusion time is performed for the equivalent nonmagnetic calculation, where the magnetic field is set to zero. It must be noted that the time-averaged  $z$  and  $s$  energies are taken from the saturated dynamo (or nonmagnetic) states, and therefore it is understood that columnar structures exist on the long timescales. The possible role of wave motions in establishing these structures from the point when energy is injected by buoyancy is not considered in this study. From Fig. 5, we find that  $\frac{1}{2} u_s^2$  and  $\frac{1}{2} u_z^2$  are higher for the dynamo run compared with the nonmagnetic run for a range of small-moderate  $l$ , while the dynamo energies fall below the nonmagnetic values above a value of  $l$ . The difference between the dynamo and nonmagnetic energies, separately shown in Figs. 5(b) and 5(d), indicates that the crossover from positive to negative  $z$ -energy difference occurs at  $l = 30$  for  $E = 1.2 \times 10^{-6}$  and  $l = 46$  for  $E = 3 \times 10^{-7}$ . (For  $E = 1.2 \times 10^{-5}$ , this crossover occurs at  $l = 18$ .) It is notable that the crossover points are close to the mean harmonic degrees of energy injection ( $l_E$ ) for these cases (see Table I). Evidently, the energy addition by the dynamo field is extended to higher  $l$  (smaller length scales) as the rotation rate is increased. The azimuthal ( $\phi$ ) energy in the dynamo runs, however, is consistently lower at all scales compared with that for the nonmagnetic runs, which suggests that the magnetic field via the Lorentz force simply damps the azimuthal energy. The analysis in this paper is hence focused on the effect of the field on the  $s$  and  $z$  flows.

The variation in  $z$ -kinetic energy over  $l$ , noted in Fig. 5, is supported by snapshots of the axial velocity  $u_z$  in the growth phase of the dynamo simulation at  $E = 1.2 \times 10^{-6}$ . The ranges  $l \leq 30$  [Figs. 6(a), 6(c) and 6(e)] and  $l > 30$  [Figs. 6(b), 6(d) and 6(f)] are shown separately. For  $l \leq 30$ , a progressive enhancement of the convective motion with time is seen, whereas scales of  $l > 30$  experience attenuation. The addition of  $z$  energy into the flow at small-moderate  $l$  and the extraction of  $z$  energy from the flow at large  $l$  accompany the growth of the magnetic field and occur well before saturation of the dynamo [see Fig. 3(a)]. The magnetic field thus acts in ways that enhance the energy of the columnar flow [14] and draw energy from the small scales through the Lorentz

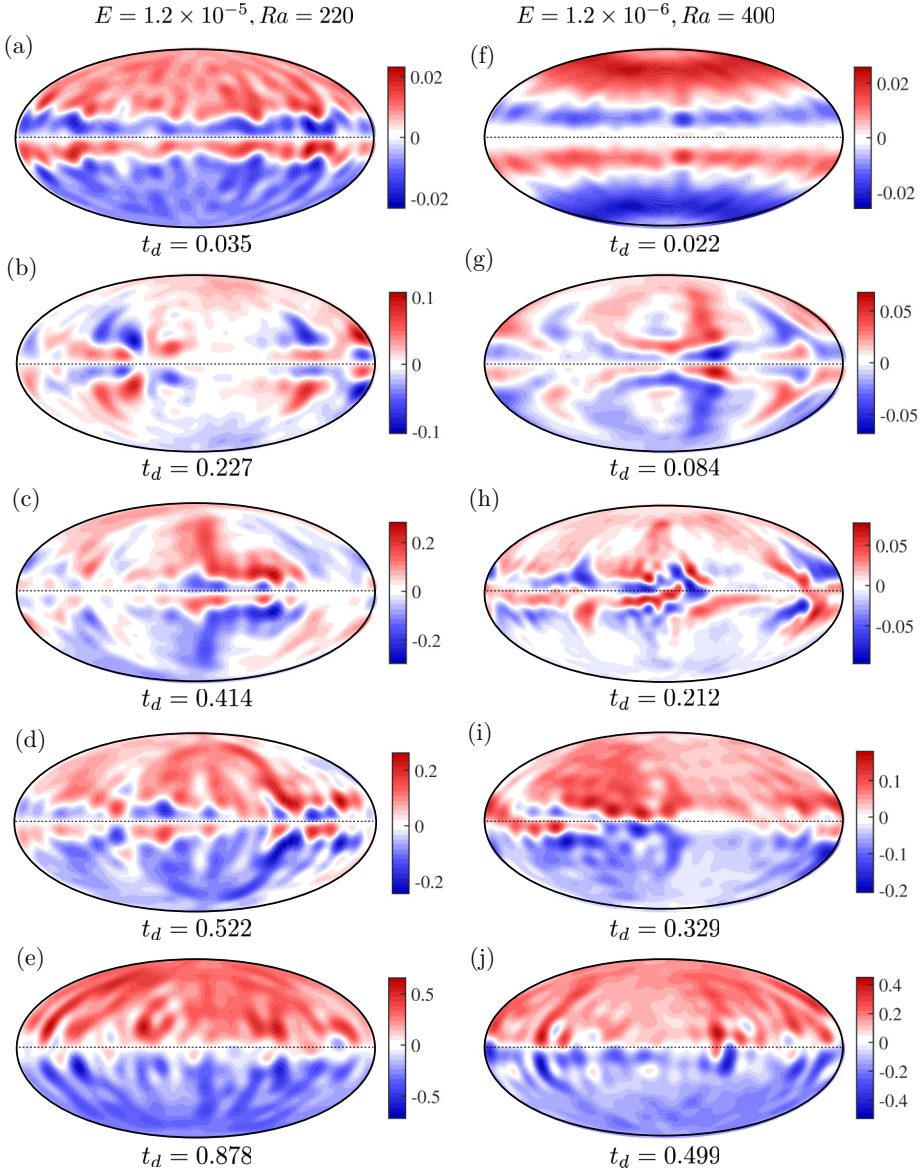


FIG. 4. Shaded contours of the radial magnetic field at the outer boundary in nonlinear dynamo simulations at two parameter regimes. The times, measured in units of the magnetic diffusion time, are taken from points on the Elsasser number plots in Fig. 3(a).

force. Interestingly, the structure of  $u_z$  does not change much after  $t_d \approx 0.32$ , which indicates that the timescale for the growth of convection intensity in the dynamo approximately coincides with the timescale for the formation of the axial dipole in the run (see video Br\_nl.avi [28]).

### B. Kinetic helicity

The variation in the  $z$  and  $s$  kinetic energies relative to their nonmagnetic values is further reflected in the kinetic helicity  $\mathbf{u} \cdot \boldsymbol{\omega}$ , with  $\boldsymbol{\omega}$  being the vorticity. In the rapidly rotating limit of  $E \rightarrow 0$ , the dominant contributions to the helicity are from  $u_z \omega_z$  and  $u_s \omega_s$  [14]. As the Ekman boundary layers

$$E = 1.2 \times 10^{-6}, Ra = 400$$

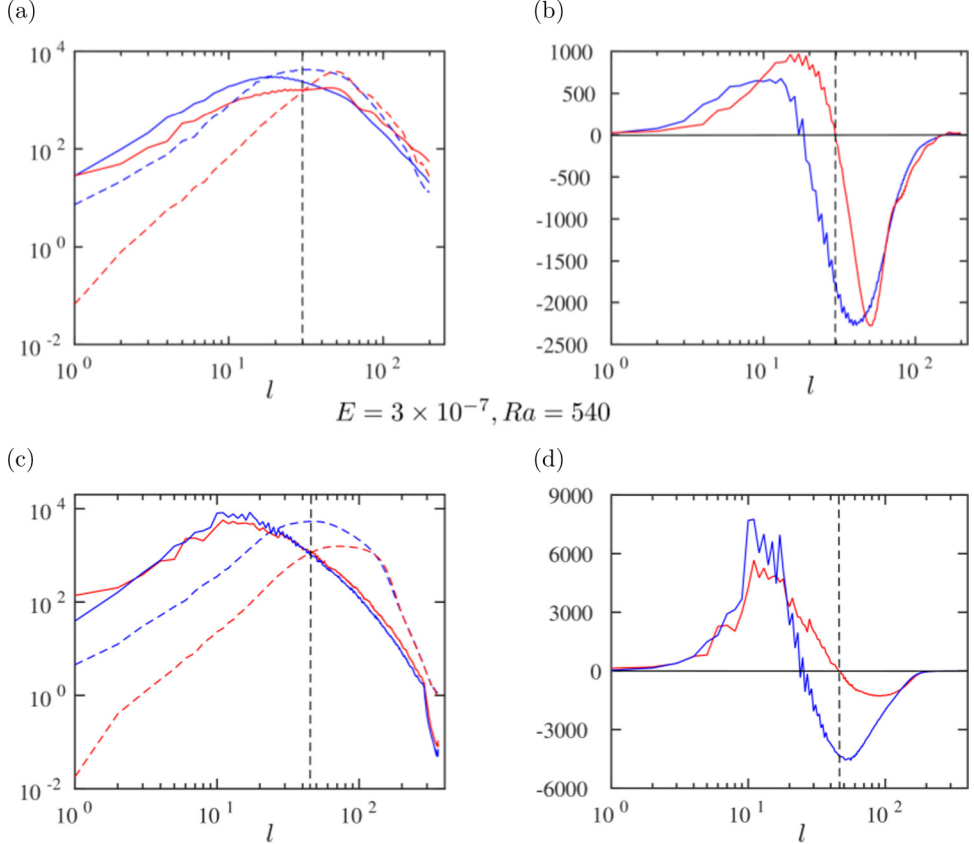


FIG. 5. (a) & (c): Variation over spherical harmonic degree  $l$  of the time-averaged kinetic energy density in the non-magnetic (dashed lines) and nonlinear dynamo (solid lines) calculations. The  $z$ -energy is shown in red and the  $s$ -energy is shown in blue. (b) & (d): The difference in  $z$ -energy density between the dynamo and non-magnetic runs (red) and the respective difference in  $s$  energy density (blue). The parameter regime ( $E, Ra$ ) considered is given above the panels.

are sources of vorticity in spherical shell models, the helicity generated in these layers needs to be filtered out in order to reveal the effect of the magnetic field on the helicity distribution in the interior (Fig. 7). We find that  $u_s\omega_s$  and  $u_z\omega_z$  are higher for the dynamo run compared with the nonmagnetic run for small-moderate  $l$ , while the dynamo helicities fall below the nonmagnetic values above a certain value of  $l$ . The difference between the dynamo and nonmagnetic helicities, separately shown in Figs. 7(b) and 7(d), indicates that the crossover from positive to negative  $z$ -helicity difference occurs at  $l = 30$  for  $E = 1.2 \times 10^{-6}$  and  $l = 46$  for  $E = 3 \times 10^{-7}$ . (For  $E = 1.2 \times 10^{-5}$ , the crossover is at  $l = 18$ .) Thus, the helicity generation by the dynamo field is extended to higher  $l$  as the rotation rate is increased. The approximate equality between the  $s$  and  $z$  dynamo helicities is predictable from linear magnetoconvection in the limit  $E \rightarrow 0$  [14] and indicates that the dynamo simulations are in the regime of rapid rotation. The decrease in helicity for  $l > 30$  ( $E = 1.2 \times 10^{-6}$ ) and  $l > 46$  ( $E = 3 \times 10^{-7}$ ) relative to the nonmagnetic calculations is a consequence of the transfer of energy from the flow at these scales into the magnetic field via the Lorentz force. The variation in  $z$  helicity over  $l$  is also seen in the time average at a section (Fig. 8). For  $E = 3 \times 10^{-7}$  and  $Ra = 540$ , the  $z$  helicity shows contrasting behaviors for two ranges of  $l$ : For  $l \leq 46$ , saturated dynamo has a considerably higher density than that in the equivalent nonmagnetic run, whereas for  $l > 46$ , the

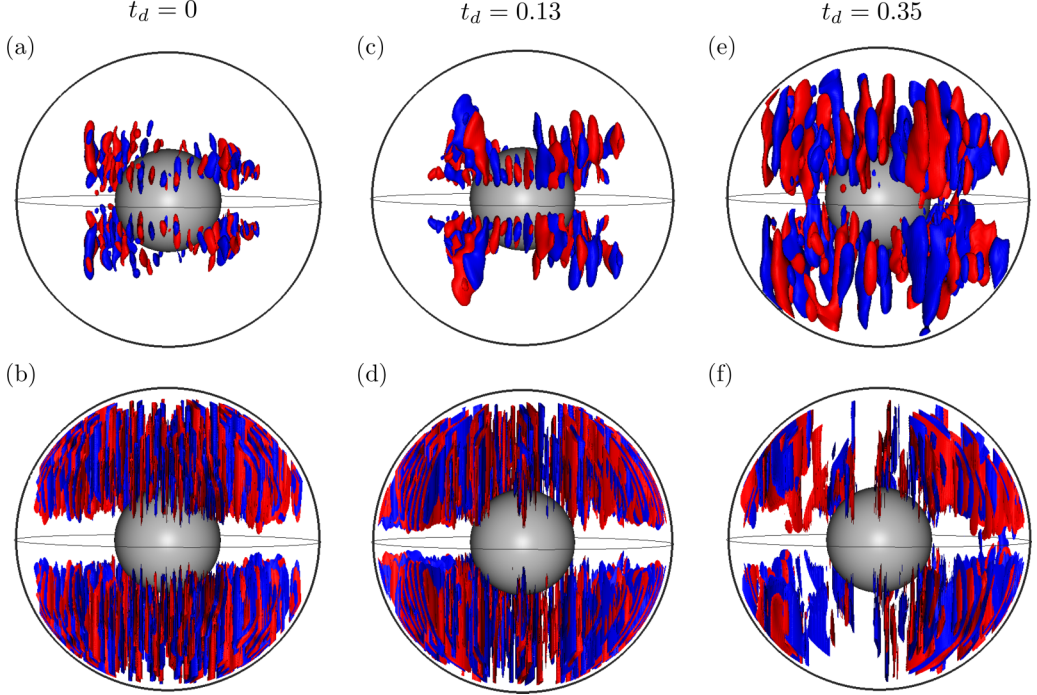


FIG. 6. Top panels [(a), (c), (e)]: Snapshots in time (measured in units of the magnetic diffusion time) of the isosurfaces of  $u_z$  (contour level  $\pm 80$ ) for  $l \leq 30$  in the nonlinear dynamo simulation. Bottom panels [(b), (d), (f)]:  $u_z$  (contour level  $\pm 150$ ) at the same times, but for  $l > 30$ . The parameters used are  $E = 1.2 \times 10^{-6}$ ,  $\text{Pr} = \text{Pm} = 1$ ,  $\text{Ra} = 400$ .

dynamo helicity is considerably sparse. The peak values themselves are not significantly different between the dynamo and nonmagnetic runs. These results confirm that the helicity generation in the dynamo is confined to the relatively large scales, while smaller scales experience loss of helicity due to the extraction of energy by the Lorentz force.

### C. Balance of terms in the vorticity equation and implications for helicity

On time and volume average, the curl of the momentum equation takes the form

$$\underbrace{\nabla \times (\nabla \times \mathbf{B}) \times \mathbf{B}}_{\text{M}} + \underbrace{q \text{Ra} \nabla \times (\mathbf{T} \mathbf{r})}_{\text{A}} + \underbrace{\partial \mathbf{u} / \partial z}_{\text{C}} - \underbrace{E \text{Pm}^{-1} \nabla \times (\boldsymbol{\omega} \times \mathbf{u})}_{\text{I}} + \underbrace{E \nabla^2 \boldsymbol{\omega}}_{\text{V}} = 0, \quad (6)$$

where  $\boldsymbol{\omega} = \nabla \times \mathbf{u}$  and  $q = \text{Pm} \text{Pr}^{-1}$ . Here the letters M, A, C, I, and V represent the magnetic (Lorentz force), Archimedean (buoyancy), Coriolis, nonlinear inertial, and viscous diffusion terms.

Figure 9 presents the time-averaged M, A, and C terms in the  $z$ -vorticity equation for the saturated nonlinear dynamo at  $E = 1.2 \times 10^{-6}$  and  $\text{Ra} = 400$ . The Lorentz (M) force term is calculated separately based on the axial dipole and nondipole parts of the magnetic field, the dipole contribution being, e.g., [29]

$$\mathbf{M}_{AD} = \nabla \times [(\nabla \times \mathbf{B}_{10}^P) \times \mathbf{B}].$$

The nondipole part of the M term is essentially derived from equatorially antisymmetric harmonics of  $\mathbf{B}^P$  other than  $\mathbf{B}_{10}^P$ . The I and V terms are not shown in the figure because these are much smaller than M, A, and C for the parameters chosen, except near the truncation wave number (also see Ref. [17]). To obtain the distribution of the terms across scales, their root mean square (rms) values

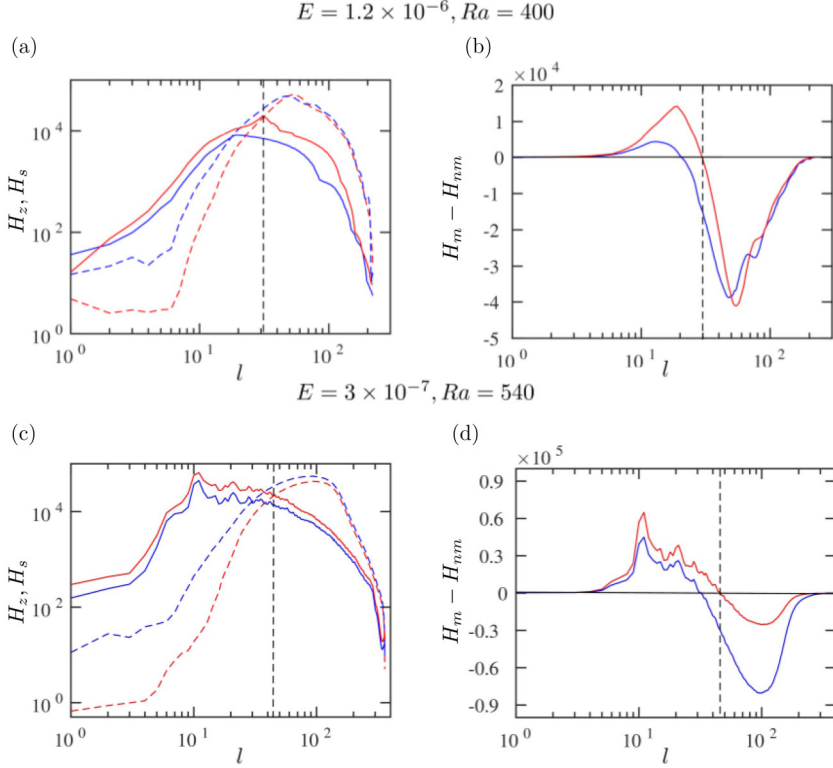


FIG. 7. [(a), (c)] Variation over the spherical harmonic degree  $l$  of the time-averaged kinetic helicity in the lower hemisphere in the nonmagnetic (dashed lines) and nonlinear dynamo (solid lines) calculations. The  $z$  helicity is shown in red and  $s$  helicity is shown in blue. [(b), (d)] The difference in  $z$  helicity between the dynamo and nonmagnetic runs (red) and the respective difference in  $s$  helicity (blue). The parameter regime ( $E$ ,  $Ra$ ) considered is given above the panels.

are given as a function of the harmonic degree,  $l$ . For  $l \leq 30$ , the dominant balance is between C (shown in red circles) and A (green line) terms. However, there is a slightly weaker contribution from M based on the nondipole field (blue line). The buoyancy term A peaks in the neighborhood of the energy injection wave number  $l_E$  and decreases steeply at small and large wave numbers. For  $l > 30$ , a nearly exact balance exists between C and the nondipole part of M. The dipole part of M (black line) is significantly smaller than the nondipole part in both ranges of  $l$ , which is not entirely surprising given that the dipole field strength (measured by  $\Lambda_D$ ) is substantially smaller than the total field strength for the Rayleigh numbers considered (Table I). As we see below, the M-C balance for  $l > 30$  causes vortex stretching, essential to the extraction of energy from these scales [see Fig. 5(b)].

To visualize the nature of the M-C balance, we first look at time-averaged contour plots of the C term  $\partial u_z / \partial z$ , interpreted as a strain rate, over two ranges of  $l$  (Fig. 10). The plots are shown on a cylindrical  $(z, \phi)$  surface. For  $l \leq 30$ , the saturated dynamo shows a global increase in the strain rate over the nonmagnetic case, consistent with the excitation of convection in regions that were quiescent in the nonmagnetic state [Figs. 6(a), 6(c) and 6(e)]. For  $l > 30$ , on the other hand, the magnetic backreaction produces bands of positive strain rate above and below the equator [Fig. 10(d)]. The magnitude of  $\partial u_z / \partial z$  is higher in Fig. 10(d) compared with Fig. 10(c), because of which these banded structures would be present if the C term were computed using the full range of  $l$  [17]. By computing C over two ranges of  $l$ , we find that the bands of positive strain rate occur only in the range  $l > 30$  where the M and C terms balance (see Fig. 9). Furthermore, the nondipole part of the

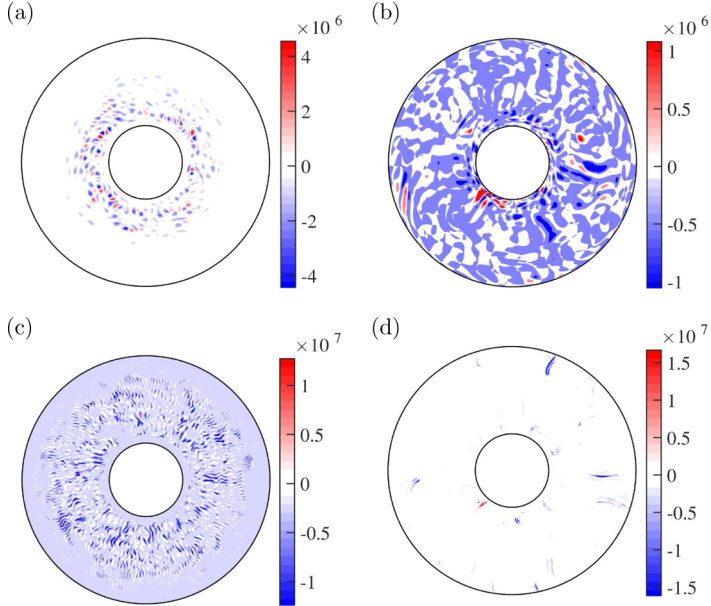


FIG. 8. Time-averaged  $z$  helicity on the section  $z = 0.3$  parallel to the equator. The parameters used in the dynamo model are  $E = 3 \times 10^{-7}$ ,  $\text{Ra} = 540$ , and  $\text{Pr} = \text{Pm} = 1$ . Panels (a) and (b) compare the respective helicities in the nonmagnetic and dynamo calculations for spherical harmonic degrees  $l \leq 46$ ; panels (c) and (d) give the same comparison for  $l > 46$ .

$M$  term [Fig. 11(b)] is in approximate balance with the  $C$  term [Fig. 10(d)] in the saturated dynamo, while  $M$  derived from the axial dipole field [Fig. 11(a)] does not contribute to this balance. It may thus be inferred that the bands of positive strain rate above and below the equator are produced by the equatorially antisymmetric harmonics of the field other than the axial dipole.

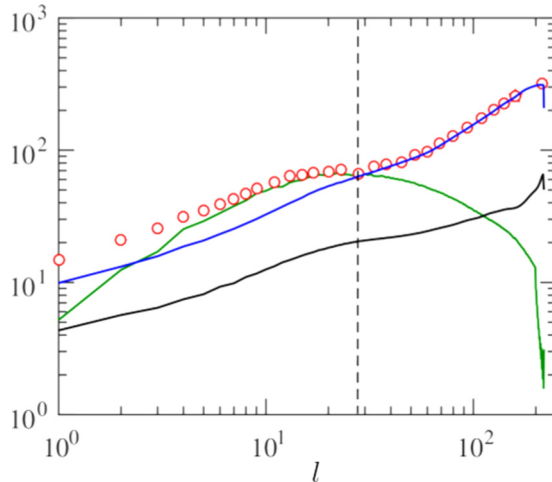


FIG. 9. Plots of the magnetic (M), buoyancy (A), and Coriolis (C) terms in the  $z$ -vorticity equation as a function of spherical harmonic degree  $l$  for the saturated nonlinear dynamo at  $E = 1.2 \times 10^{-6}$ ,  $\text{Ra} = 400$ , and  $\text{Pr} = \text{Pm} = 1$ . The line styles used are the following: C (red circles), A (green line), M based on the axial dipole field only (black line), and M based on the nondipole field (blue line).

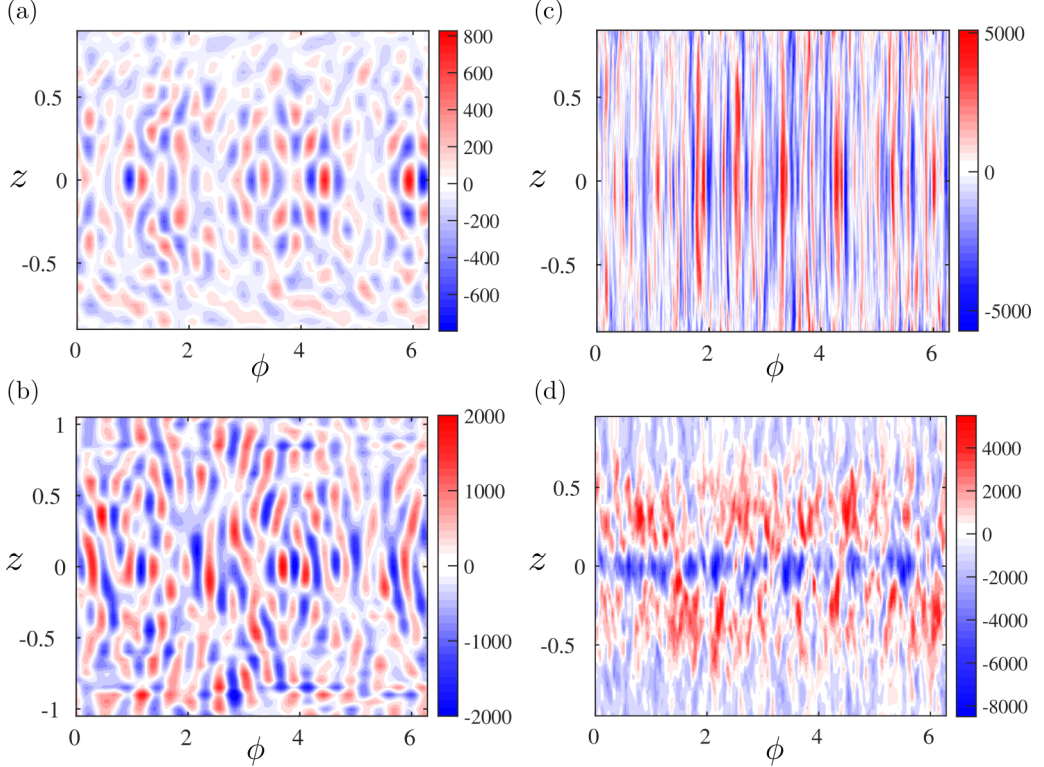


FIG. 10. Contour plots of the time-averaged Coriolis (C) term in the  $z$ -vorticity equation shown on a cylinder of radius  $s = 1.1$ . The parameters used in the dynamo simulation are  $E = 1.2 \times 10^{-6}$ ,  $\text{Ra} = 400$ ,  $\text{Pr} = \text{Pm} = 1$ . Two ranges of the spherical harmonic degree are considered: [(a), (b)]  $l \leq 30$ ; [(c), (d)]  $l > 30$ . The upper panels (a) and (c) represent nonmagnetic convection and the lower panels (b) and (d) represent the saturated dynamo.

A consequence of the generation of bands of positive strain rate  $C$  is the marked asymmetry between cyclones and anticyclones [17], which does not exist in nonmagnetic convection at small Rossby number. Since  $\partial u_z / \partial z > 0$  in anticyclones and  $< 0$  in cyclones in the neighborhood of the equator [16], the generation of positive  $\partial u_z / \partial z$  by the damping Lorentz force substantially weakens cyclonic vortices. By considering scale dependence of the kinetic helicity, the picture obtained from earlier studies (e.g., Ref. [17]), which do not consider scale-dependent dynamics, is now further refined: In the range  $l \leq 30$ , the dynamo helicity is enhanced in both cyclones and anticyclones relative to the nonmagnetic helicity; for  $l > 30$ , however, the cyclonic helicity in the dynamo is preferentially attenuated relative to its nonmagnetic value, producing a vortex asymmetry (Fig. 12).

#### D. Toroidal field generation

The mechanism of generation of the toroidal part of the axial dipole ( $\mathbf{B}_{20}^T$ ) may be understood by calculating the integral energy contribution to this component (e.g., Ref. [30]),

$$\Gamma_{20}^T = \int_V \mathbf{B}_{20}^T \cdot \nabla \times (\mathbf{u} \times \mathbf{B}) dV, \quad (7)$$

where  $(\mathbf{u} \times \mathbf{B})$  can have contributions from  $(\mathbf{u}^T \times \mathbf{B}^P)$ ,  $(\mathbf{u}^P \times \mathbf{B}^T)$ ,  $(\mathbf{u}^T \times \mathbf{B}^T)$ , and  $(\mathbf{u}^P \times \mathbf{B}^P)$ . Denoting the harmonic indices of  $\mathbf{u}$ ,  $\mathbf{B}$ , and  $\mathbf{B}_{20}^T$  by  $\alpha$ ,  $\beta$ , and  $\gamma$ , respectively, the harmonic selection rule [31] prescribes  $m_\alpha = m_\beta$  for  $m_\gamma = 0$ , which simplifies the evaluation of (7). From Fig. 13(a), we note that  $(\mathbf{u}^T \times \mathbf{B}^P)$  makes the dominant positive contribution to  $\Gamma_{20}^T$ , and this contribution essentially

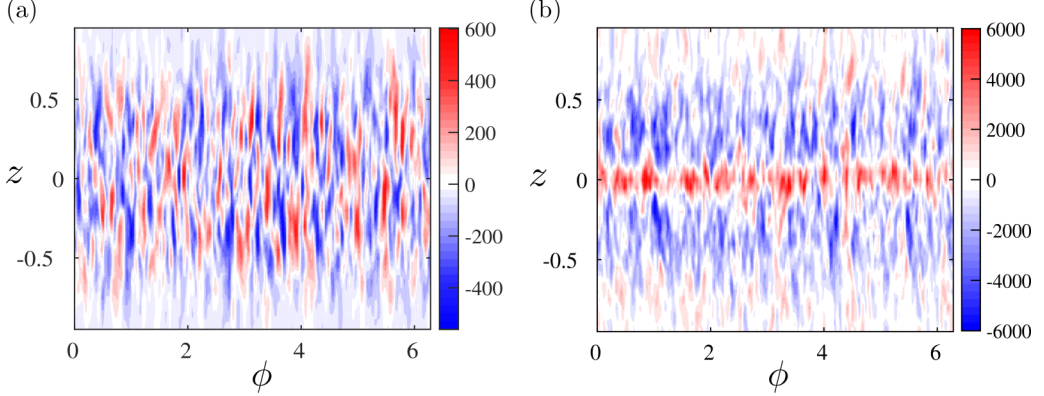


FIG. 11. Contour plots of the time-averaged Lorentz (M) term in the  $z$ -vorticity equation shown on a cylinder of radius  $s = 1.1$ . The parameters used in the dynamo simulation are  $E = 1.2 \times 10^{-6}$ ,  $\text{Ra} = 220$ ,  $\text{Pr} = \text{Pm} = 1$ . Panels (a) and (b) show the M term based on the axial dipole and nondipole parts of the field respectively.

comes from the  $m = 0$  components of both  $\mathbf{u}^T$  and  $\mathbf{B}^P$ . Further,  $(l_\alpha, l_\beta)$  can have the combinations (1,1), (3,1), (2,2), and (4,2). [Note, for example, that (2,1) is not possible as  $l_\alpha + l_\beta + l_\gamma$  is odd.] From the energy matrices of  $\nabla \times (\mathbf{u}^T \times \mathbf{B}^P)$  for  $m_\alpha = m_\beta = 0$  at two times in the growth phase of the field [Figs. 13(b) and 13(c)], we note that  $l_\alpha$  switches from 1 to 3 while  $l_\beta = 1$ . At the first of these times,  $t_d = 0.414$ , the radial field at the outer boundary is chaotic [Fig. 4(c)]; at  $t_d = 0.522$ , the dipole structure appears [Fig. 4(d)]. The effect of the magnetic backreaction is visible in the comparison of the time-averaged zonal flows of the nonmagnetic and saturated dynamo states [Figs. 14(a) and 14(b)]:

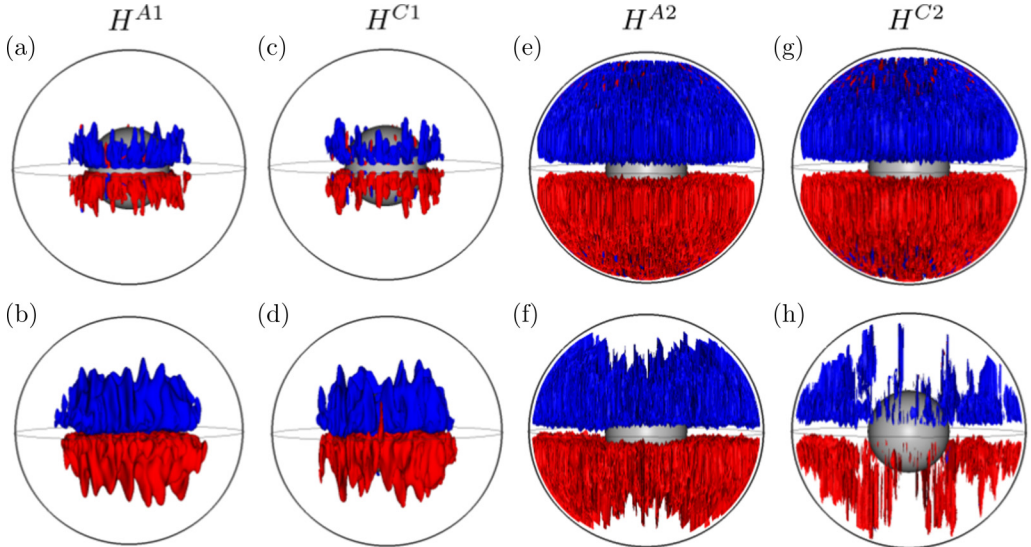


FIG. 12. Upper panels [(a), (c), (e), (g)] show isosurfaces of the time-averaged anticyclonic (A) and cyclonic (C)  $z$  helicity for nonmagnetic convection. Lower panels [(b), (d), (f), (h)] show the respective plots for the saturated (nonlinear) dynamo. Two ranges of the spherical harmonic degree are considered: (a)–(d)  $l \leq 30$ , shown at contour levels  $\pm 2 \times 10^4$ , and (e)–(h)  $l > 30$ , shown at contour levels  $\pm 2 \times 10^5$ . The parameters used in the dynamo model are  $E = 1.2 \times 10^{-6}$ ,  $\text{Pr} = \text{Pm} = 1$ , and  $\text{Ra} = 400$ .

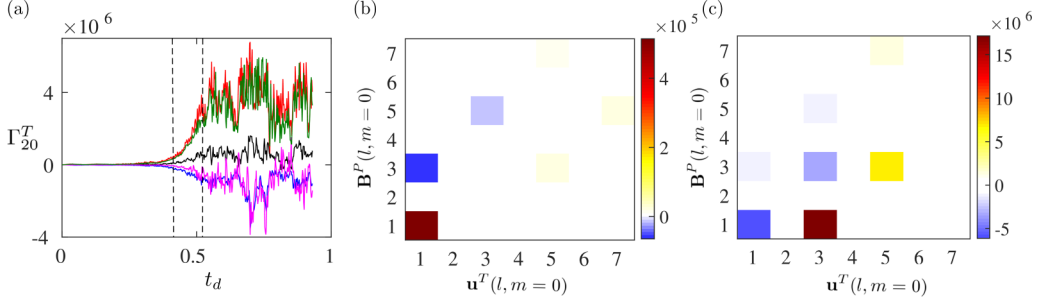


FIG. 13. (a) Volume integral of induction term dotted with  $\mathbf{B}_{20}^T$ . The line colors are red,  $\nabla \times (\mathbf{u}^T \times \mathbf{B}^P)$ ; blue,  $\nabla \times (\mathbf{u}^P \times \mathbf{B}^T)$ ; black,  $\nabla \times (\mathbf{u}^P \times \mathbf{B}^P)$ ; magenta,  $\nabla \times (\mathbf{u}^T \times \mathbf{B}^T)$ ; and green,  $\nabla \times (\mathbf{u}_{m=0}^T \times \mathbf{B}_{m=0}^P)$ . Panels (b) and (c) give the energy matrix for  $\nabla \times (\mathbf{u}_{m=0}^T \times \mathbf{B}_{m=0}^P)$  at two different times,  $t_d = 0.414$  and  $t_d = 0.522$  respectively, shown by dashed vertical lines in panel (a). The parameters used in the simulation are  $E = 1.2 \times 10^{-5}$ ,  $\text{Ra} = 220$ , and  $\text{Pr} = \text{Pm} = 5$ .

The  $Y_1^0$  pattern in the nonmagnetic state gives way to the layered  $Y_3^0$  pattern in the saturated dynamo, thus localizing strong anticyclonic vortices in the polar regions.

#### IV. CONCLUSION

This paper investigates the scale dependence of the magnetic backreaction and its likely role in the selection of the axial dipole in rapidly rotating spherical dynamos. The motivation for the present study stems from the dipole dominance of planetary magnetic fields such as Earth's, although changes in convection strength can cause interruptions to this axial dipole state (e.g., Refs. [32,33]). The Rayleigh number for convection is chosen such that the axial dipole grows from a starting seed field in the nonlinear dynamo, but does not pick up strength in the kinematic dynamo at the same parameters. At the lower Rayleigh numbers (e.g.,  $\text{Ra} = 2.5\text{--}3 \times \text{Ra}_c$  at  $E = 1.2 \times 10^{-5}$ ), the equatorial symmetry of the velocity field that arises from rotation ( $[u_r, u_\theta, u_\phi](r, \theta, \phi) = [u_r, -u_\theta, u_\phi](r, \pi - \theta, \phi)$ ) is exact, so that the symmetry of the starting magnetic field determines its subsequent evolution. Here, the dipole component  $\mathbf{B}_{10}^P$  grows from its small seed value ( $\Lambda = 0.01$ ) in both the nonlinear and kinematic runs (Fig. 2). For a pure quadrupole seed field start, the magnetic energy simply decays in time in both the nonlinear and kinematic runs since the  $z$  velocity is zero on the equatorial plane where  $B_\phi$  is maximum. Even if the initial seed field consists of a mix of 99.99% quadrupole and 0.01% dipole components, the eventual state is an axial dipole, although a longer time is needed to attain that state. Having understood that the polarity of the starting seed field determines the

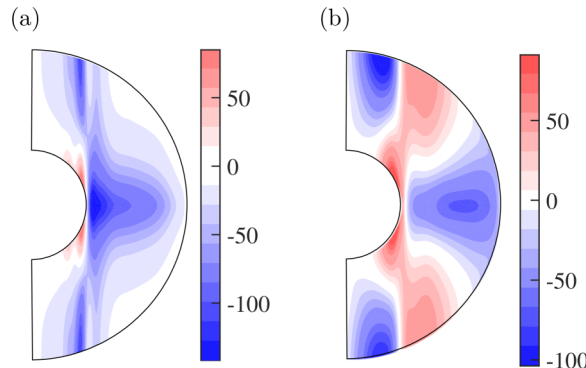


FIG. 14. Meridional plots of time and azimuthally averaged  $\phi$  velocity in the calculation at  $E = 1.2 \times 10^{-5}$ ,  $\text{Ra} = 220$ , and  $\text{Pr} = \text{Pm} = 5$ . (a) Nonmagnetic state; (b) saturated nonlinear dynamo.

evolution of the dynamo at low Ra, we move to still supercritical convection, which is the focus of this paper. In this regime, the polarity of the starting field has no bearing on the final polarity, which is characterized by the axial dipole. Although a starting field of mixed polarity does not alter the final state of the dynamo, an axial dipole is chosen as the initial state so that its evolution with and without the magnetic backreaction may be followed. For the case of highly supercritical convection ( $\text{Ra} \gg \text{Ra}_c$ ) not considered in this paper, a seed field may grow into a chaotic field with no well-defined polarity [14]. However, early Earth's dynamo is thought to have been powered solely by thermal convection arising from secular cooling of the core [34], so that the early growth of the geomagnetic field probably occurred under moderately supercritical convection.

As the field grows from its initial seed dipole state, it loses its dipole character in the early stages of evolution where the Lorentz force is weak, but subsequently regains it well before dynamo saturation. The backreaction of the field produces a substantial variation in the intensity of convection across length scales, relative to the reference nonmagnetic state. As a result, the large-scale region of the spectrum has helicity generation, whereas the region of relatively small scales from which energy is drawn by the Lorentz force has helicity deficit. Decreasing  $E$  from  $1.2 \times 10^{-5}$  to  $3 \times 10^{-7}$  displaces the crossover point between the two regions to smaller length scales. In other words, helicity is generated at progressively smaller scales as the Ekman number is lowered, indicating the influence of rotation on these scales. Given that the timescale for the growth in convection intensity [Figs. 6(a), 6(c) and 6(e)] roughly coincides with the timescale for the formation of the axial dipole, it is reasonable to suppose that the dipole field is aided by the field-induced helicity.

One aspect in which supercritical dynamos differ from near-critical dynamos is that the nondipole part of the field is much stronger than the dipole part, so that the Lorentz force based on the nondipole field makes the main contribution to the M-C balance in the small-scale region of the dynamo spectrum (e.g.,  $l > 30$  in Fig. 9). These scales may be important for the generation of slow magnetostrophic waves in the Earth's core [35]. The fact that the magnetic field can set up convection at the relatively large length scales where the Lorentz (M) force is weaker than the A and C forces is reasonable in view of the onset of plane magnetoconvection under spatially inhomogeneous weak fields [19]. However, since stationary onset models reproduce only the long-time columnar structure of the convection, one needs to reinstate the time derivatives of the velocity and the induced magnetic field to know whether fast inertial waves weakly modified by the Lorentz force [35,36] can excite convection during the growth phase of the dynamo.

This study also examines the generation of the toroidal part of the dipole,  $\mathbf{B}_{20}^T$ . Here, the classical  $\Omega$  effect holds, where the axial dipole field is sheared by differential rotation. At near-critical Ra, the zonal flow has a  $Y_1^0$  pattern in both the kinematic and nonlinear regimes, which implies that the Lorentz force is not strong enough to produce a backreaction. At progressively higher Ra, the zonal flow switches from the  $Y_1^0$  to the  $Y_3^0$  pattern as the magnetic field grows in time.

#### ACKNOWLEDGMENTS

B.S. was awarded a SwarnaJayanti Fellowship by the Department of Science and Technology (India) during this project. This study was supported in part by Research Grant No. 5307-1 awarded by the Indo-French Centre for the Promotion of Advanced Research (IFCPAR). The computations were performed on SahasraT, the supercomputer at IISc Bangalore. B.S. acknowledges the help of Aditya Varma in verifying the analysis for Table I. Thanks are given to the anonymous referees for their constructive reviews.

---

- [1] C. A. Jones, Thermal and compositional convection in the outer core, in *Core Dynamics*, edited by P. Olson, Treatise on Geophysics Vol. 8 (Elsevier, Amsterdam, 2015), pp. 115–159.
- [2] U. R. Christensen and J. Wicht, Numerical dynamo simulations, in *Core Dynamics*, edited by P. Olson, Treatise on Geophysics Vol. 8 (Elsevier, Amsterdam, 2015), pp. 245–277.

- [3] E. Grote, F. H. Busse, and A. Tilgner, Regular and chaotic spherical dynamos, *Phys. Earth Planet. Inter.* **117**, 259 (2000).
- [4] F. H. Busse and R. D. Simitev, Parameter dependences of convection-driven dynamos in rotating spherical fluid shells, *Geophys. Astrophys. Fluid Dyn.* **100**, 341 (2006).
- [5] N. Ishihara and S. Kida, Equatorial magnetic field intensification by convection vortices in a rotating spherical shell, *Fluid Dyn. Res.* **31**, 253 (2002).
- [6] J. Aubert and J. Wicht, Axial vs. equatorial dipolar dynamo models with implications for planetary magnetic fields, *Earth Planet. Sci. Lett.* **221**, 409 (2004).
- [7] B. Sreenivasan and C. A. Jones, The role of inertia in the evolution of spherical dynamos, *Geophys. J. Int.* **164**, 467 (2006).
- [8] R. K. Yadav, T. Gastine, U. R. Christensen, S. J. Wolk, and K. Poppenhaeger, Approaching a realistic force balance in geodynamo simulations, *Proc. Natl. Acad. Sci. USA* **113**, 12065 (2016).
- [9] N. Schaeffer, D. Jault, H.-C. Nataf, and A. Fournier, Turbulent geodynamo simulations: A leap towards Earth's core, *Geophys. J. Int.* **211**, 1 (2017).
- [10] P. H. Roberts, On the thermal instability of a rotating fluid sphere containing heat sources, *Phil. Trans. R. Soc. London, Ser. A* **263**, 93 (1968).
- [11] K. Zhang, Spiralling columnar convection in rapidly rotating spherical fluid shells, *J. Fluid Mech.* **236**, 535 (1992).
- [12] D. Gubbins, C. N. Barber, S. Gibbons, and J. J. Love, Kinematic dynamo action in a sphere. I. Effects of differential rotation and meridional circulation on solutions with axial dipole symmetry, *Proc. R. Soc. London, Ser. A* **456**, 1333 (2000).
- [13] N. Schaffer and P. Cardin, Quasi-geostrophic kinematic dynamos at low magnetic Prandtl number, *Earth Planet. Sci. Lett.* **245**, 595 (2006).
- [14] B. Sreenivasan and C. A. Jones, Helicity generation and subcritical behavior in rapidly rotating dynamos, *J. Fluid Mech.* **688**, 5 (2011).
- [15] H. K. Moffatt, *Magnetic Field Generation in Electrically Conducting Fluids* (Cambridge University Press, Cambridge, UK, 1978).
- [16] P. Olson, U. R. Christensen, and G. A. Glatzmaier, Numerical modeling of the geodynamo: Mechanism of field generation and equilibration, *J. Geophys. Res.* **104**, 10383 (1999).
- [17] B. Sreenivasan, S. Sahoo, and G. Dham, The role of buoyancy in polarity reversals of the geodynamo, *Geophys. J. Int.* **199**, 1698 (2014).
- [18] K. M. Soderlund, E. M. King, and J. Aurnou, The influence of magnetic fields in planetary dynamo models, *Earth Planet. Sci. Lett.* **333–334**, 9 (2012).
- [19] B. Sreenivasan and V. Gopinath, Confinement of rotating convection by a laterally varying magnetic field, *J. Fluid Mech.* **822**, 590 (2017).
- [20] J. Aubert, T. Gastine, and A. Fournier, Spherical convective dynamos in the rapidly rotating asymptotic regime, *J. Fluid Mech.* **813**, 558 (2017).
- [21] J. M. Aurnou and E. M. King, The cross-over to magnetostrophic convection in planetary dynamo systems, *Proc. R. Soc. London, Ser. A.* **473**, 20160731 (2017).
- [22] S. I. Braginsky and P. H. Roberts, Equations governing convection in Earth's core and the geodynamo, *Geophys. Astrophys. Fluid Dyn.* **79**, 1 (1995).
- [23] M. Kono and P. H. Roberts, Recent geodynamo simulations and observations of the geomagnetic field, *Rev. Geophys.* **40**, 101 (2002).
- [24] A. P. Willis, B. Sreenivasan, and D. Gubbins, Thermal core-mantle interaction: Exploring regimes for “locked” dynamo action, *Phys. Earth Planet. Inter.* **165**, 83 (2007).
- [25] U. R. Christensen and J. Aubert, Scaling properties of convection-driven dynamos in rotating spherical shells and application to planetary magnetic fields, *Geophys. J. Int.* **166**, 97 (2006).
- [26] J. Rotvig and C. A. Jones, Rotating convection-driven dynamos at low Ekman number, *Phys. Rev. E* **66**, 056308 (2002).
- [27] See Supplemental Material at <http://link.aps.org/supplemental/10.1103/PhysRevFluids.3.093801> for a video of the evolution of the radial magnetic field in a kinematic dynamo simulation.

- [28] See Supplemental Material at <http://link.aps.org/supplemental/10.1103/PhysRevFluids.3.093801> for a video of the evolution of the radial magnetic field in a nonlinear dynamo simulation.
- [29] F. Takahashi and H. Shimizu, A detailed analysis of a dynamo mechanism in a rapidly rotating spherical shell, *J. Fluid Mech.* **701**, 228 (2012).
- [30] B. A. Buffett and J. Bloxham, Energetics of numerical dynamo models, *Geophys. J. Int.* **149**, 211 (2002).
- [31] E. Bullard and H. Gellman, Homogeneous dynamos and terrestrial magnetism, *Philos. Trans. R. Soc. London, Ser. A* **247**, 213 (1954).
- [32] K. Zhang, Spherical shell rotating convection in the presence of a toroidal magnetic field, *Proc. R. Soc. London, Ser. A* **448**, 245 (1995).
- [33] K. Zhang and D. Gubbins, Is the geodynamo process intrinsically unstable?, *Geophys. J. Int.* **140**, F1 (2000).
- [34] S. Sahoo, B. Sreenivasan, and H. Amit, Dynamos driven by weak thermal convection and heterogeneous outer boundary heat flux, *Phys. Earth Planet. Inter.* **250**, 35 (2016).
- [35] B. Sreenivasan and G. Narasimhan, Damping of magnetohydrodynamic waves in a rotating fluid, *J. Fluid Mech.* **828**, 867 (2017).
- [36] D. J. Acheson and R. Hide, Hydromagnetics of rotating fluids, *Rep. Prog. Phys.* **36**, 159 (1973).